Multiple Sequential Ionization of Valence n = 4 Shell of Krypton by Intense Femtosecond XUV Pulses

Elena V. Gryzlova [1], **Maksim D. Kiselev [1,2]**, **Maria M. Popova [1,2]**, **Anton A. Zubekhin [2]**, **Giuseppe Sansone [3]** and **Alexei N. Grum-Grzhimailo [1,*]**

[1] Skobeltsyn Institute of Nuclear Physics, Lomonosov Moscow State University, 119991 Moscow, Russia; gryzlova@gmail.com (E.V.G.); md.kiselev94@gmail.com (M.D.K.); mm.popova@physics.msu.ru (M.M.P.)
[2] Physical Department, Lomonosov Moscow State University, 119991 Moscow, Russia; anton-zubehin@mail.ru
[3] Physikalisches Institut, Albert-Ludwigs-Universität Freiburg Hermann-Herder-Straße 3, 79104 Freiburg, Germany; giuseppe.sansone@physik.uni-freiburg.de
* Correspondence: grum@sinp.msu.ru; Tel.: +7-495-939-4776

Abstract: Sequential photoionization of krypton by intense extreme ultraviolet femtosecond pulses is studied theoretically for the photon energies below the 3d excitation threshold. This regime with energetically forbidden Auger decay is characterized by special features, such as time scaling of the level population. The model is based on the solution of rate equations with photoionization cross sections of krypton in different charge and multiplet states determined using R-matrix calculations. Predictions of the ion yields and photoelectron spectra for various photon fluence are presented and discussed.

Keywords: photoionization; multiple ionization; ions; free-electron laser; krypton; femtosecond pulses; photoelectron spectroscopy

1. Introduction

Multiple ionization of atoms by intense pulses generated by free-electron laser (FEL) operating in the extreme ultraviolet (XUV) has been observed since the first experiments at the Free-electron LASer in Hamburg (FLASH) [1]. Such studies are of great importance to benchmark theoretical models for the description of simple non-linear process in the XUV. Two regimes can be distinguished in the multiple ionization process:
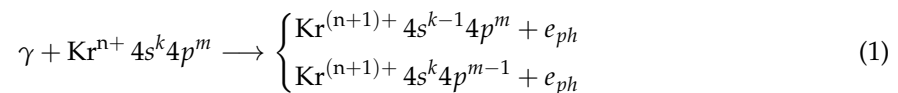
(i) The photon energy of the FEL is high enough to eject an electron from an inner shell. Within a few femtoseconds the hole is filled by an electron originating from an outer shell, through a single or cascaded Auger decay mechanism. The ultrafast dynamics of the Auger decay competes with the absorption by the target ion of another photon from the same femtosecond FEL pulse. Therefore, ionization of the target often proceeds through a chain of consecutive photoionization and Auger decay events [2]. Usually, the ion yields of the different charge states are measured in the experiment as a function of the FEL pulse parameters and they are compared with the corresponding predictions of theoretical models [3,4]. So far, only a limited number of electronic spectra in this regime have been reported in the literature [2,5].

(ii) The photon energy is not enough for creating a hole in an inner shell and therefore, the Auger process is energetically forbidden, if multiphoton ionisation is neglected. The atom is then ionized only by sequential absorption of photons by valence electrons as far as it is energetically allowed. Sequential photoionization in this regime was observed in noble gases [6–10] and the experimental results were compared with theoretical predictions [11–14]. For these processes,

in addition to the ion yield and photoelectron spectra, also the angular distribution and even angular correlation [6,12,15,16] of two emitted electrons were studied both experimentally and theoretically. The important role of autoionizing resonances was also investigated [10,17,18]. To the best of our knowledge, no studies investigating multiple ionization beyond triple charged ions in the (ii) regime has been reported so far, except a general theoretical formulation for the photoelectron angular distributions in [19].

The current study belongs to the class (ii). Our main purpose is to analyse theoretically and make predictions for sequential ionization of Kr at photon energies in the interval 50–80 eV, i.e., below the excitation threshold of the $3d$-hole (91.2 eV [20]). In this energy interval the $3d$-hole is not produced and the Auger decay is excluded. In the next section we describe the process and outline a theoretical approach for modelling the interaction based on the solution of a system of rate equations. In Section 3, we present the results focusing on the time eVolution of the atomic Kr target under the FEL pulse and on the resulting electron spectra. In Section 4 a method for calculating the photoionization cross sections required for the rate equations is described. Examples of the ionization cross sections between electronic multiplet of different charge states of Kr are presented. The last section contains our conclusions.

2. Process Description

Since the Auger decay is energetically forbidden, the main processes, which we consider are photoionization from either the $4s$ or the $4p$ energy levels with emission of a photoelectron e_{ph}

$$\gamma + \mathrm{Kr}^{n+}\, 4s^k 4p^m \longrightarrow \begin{cases} \mathrm{Kr}^{(n+1)+}\, 4s^{k-1} 4p^m + e_{ph} \\ \mathrm{Kr}^{(n+1)+}\, 4s^k 4p^{m-1} + e_{ph} \end{cases} \tag{1}$$

or radiative transition from the $4p$ to the $4s$ level with emission of a fluorescence photon γ_{fl}

$$\mathrm{Kr}^{n+}\, 4s^k 4p^m \longrightarrow \mathrm{Kr}^{n+}\, 4s^{k+1} 4p^{m-1} + \gamma_{fl} \tag{2}$$
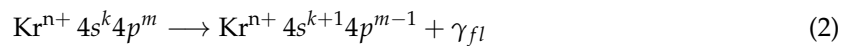
Sequential ionization of the valence shells of Kr and its ions is schematically shown in Figure 1, where ionization paths between the ionic configurations from neutral Kr to the triply charged ion Kr^{3+} are indicated. "Horizontal" radiation transitions occur between energy levels of a same ion. In fact each indicated level includes all possible multiplet states of the configuration, which were all taken into account in the calculations. For photon energies equal or lower than 50.85 eV, ionization from the $\mathrm{Kr}^{3+}\, 4s^k 4p^m$ electron configurations is energetically forbidden. For energies between 50.85 eV and 80 eV ionization channels of $\mathrm{Kr}^{3+}\, 4s^k 4p^m$ are allowed, but we neglect them (see below). Thus, we consider the sequential ionization up to triple, three-photon ionization and the scheme in Figure 1 is restricted to transitions up to Kr^{3+}. We do not consider the fine-structure levels of the multiplet states and consider summations over the fine-structure levels. This approach implies that the spectral width of the FEL pulse and resolution of the electron detector are comparable with the fine-structure splitting of the ions: $4s^2 4p^5\, {}^2P^o$ (0.65 eV), $4s^2 4p^4\, {}^3P$ (0.66 eV), $4s^1 4p^5\, {}^3P^o$ (0.69 eV), $4s^2 4p^4\, {}^2D$ (0.20 eV), $4s^2 4p^3\, {}^2P^o$ (0.39 eV), $4s^1 4p^4\, {}^4P$ (0.66 eV), $4s^1 4p^4\, {}^2D$ (0.11 eV), $4s^1 4p^4\, {}^2P$ (0.34 eV). More details on the transitions between the multiplet states in the first three ionization steps from Kr to Kr^{3+} are presented in Table 1.
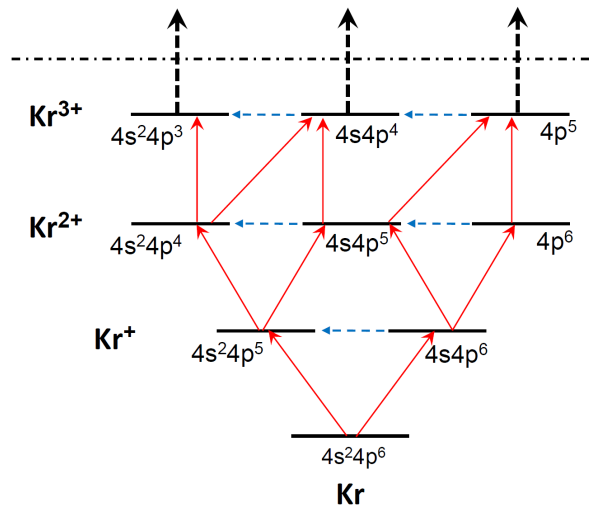
Figure 1. Scheme of transitions in sequential multiphoton ionization of Kr. Solid red arrows—photoionization, dashed blue arrows—radiative transitions. Only configurations are shown without multiplet splitting. The horizontal dash-dotted line indicates the limit for the sequential three-photon triple ionization (see text).

Table 1. List of transitions in sequential three-photon ionization of Kr. Columns and lines correspond to initial and final states of the transitions within the LS-coupling scheme, respectively. Capital letters denote photoelectron lines for further convenience. Numbers after the letters present experimental ionization thresholds [21] for the corresponding transitions in eV, averaged over a multiplet. Transitions not marked by a capital letter are weak and their contribution to the photoelectron spectra is negligible, although they are included in Equations (3).

N	Final State \\ Initial State	$4s^24p^6\,^1S$	$4s^24p^5\,^2P^o$	$4s^14p^6\,^2S$	$4s^24p^4\,^3P$	$4s^24p^4\,^1D$	$4s^24p^4\,^1S$	$4s^14p^5\,^3P^o$	$4s^14p^5\,^1P^o$	$4s^04p^6\,^1S$
1	$4s^24p^6\,^1S$	-	-	-	-	-	-	-	-	-
2	$4s^24p^5\,^2P^o$	A, 14.0	-	-	-	-	-	-	-	-
3	$4s^14p^6\,^2S$	E, 27.5	-	-	-	-	-	-	-	-
4	$4s^24p^4\,^3P$	-	B, 24.4	-	-	-	-	-	-	-
5	$4s^24p^4\,^1D$	-	D, 26.2	-	-	-	-	-	-	-
6	$4s^24p^4\,^1S$	-	F, 28.5	-	-	-	-	-	-	-
7	$4s^14p^5\,^3P^o$	-	I, 38.7	C, 25.2	-	-	-	-	-	-
8	$4s^14p^5\,^1P^o$	-	K, 42.0	F, 28.4	-	-	-	-	-	-
9	$4s^04p^6\,^1S$	-	-	K, 42.1	-	-	-	-	-	-
10	$4s^24p^3\,^4S^o$	-	-	-	G, 35.8	-	-	-	-	-
11	$4s^24p^3\,^2D^o$	-	-	-	I, 38.0	G, 36.1	33.8	-	-	-
12	$4s^24p^3\,^2P^o$	-	-	-	J, 39.7	H, 37.9	G, 35.6	-	-	-
13	$4s^14p^4\,^4P$	-	-	-	L, 50.6	-	-	G, 35.5	-	-
14	$4s^14p^4\,^2D$	-	-	-	O, 53.9	M, 52.1	49.8	I, 38.8	G, 36.3	-
15	$4s^14p^4\,^2S$	-	-	-	R, 57.4	55.6	53.3	K, 42.3	J, 39.8	-
16	$4s^14p^4\,^2P$	-	-	-	Q, 56.4	P, 54.6	M, 52.3	K, 41.4	I, 38.8	-
17	$4s^04p^5\,^2P^o$	-	-	-	-	-	-	P, 54.9	M, 52.3	I, 38.7

To follow the dynamics of the state populations, we apply a method of solving rate equations extensively used in the description of sequential ionization of atoms by X-ray FEL pulses (for example [22–29]). For femtosecond pulses the radiative $4p \rightarrow 4s$ transitions can be neglected and the temporal dynamics is dominated by photoionization.

The rate equations for the level populations then take the form (we use atomic units until otherwise indicated)

$$\frac{dN_i(t)}{dt} = j(t) \sum_{j \neq i} \left[\sigma_{j \rightarrow i} N_j(t) - \sigma_{i \rightarrow j} N_i(t) \right], \qquad i, j = 1, 2, ..., M \tag{3}$$

where $N_i(t)$ is the population of level i, $\sigma_{i \to j}$ is the photoionization cross section from level i of Kr^{n+} to level j of $\text{Kr}^{(n+1)+}$, and $j(t)$ is the intensity of the incident radiation, which varies with time according to the pulse shape. M is the number of states, which are accounted for in treating the temporal dynamics of the sequential ionization. In our case $M = 17$ according to Table 1. In the set (3) we do not include shake-up and one-photon double ionization channels [30], but account for the shake-up, as well as autoionizing resonances in the calculation of the photoionization cross sections $\sigma_{i \to j}$. Details of the cross section calculations are presented in Section 4.

The discrete levels can influence the process through two-photon resonance single ionization [31,32]. Photon energies above 50 eV, are above the $4s$ and $4p$ ionization thresholds in Kr and Kr^+ and therefore the two-photon resonance ionization via their discrete states is not possible. However, for energies around 50 eV, the channel of one-photon ionization of the $4s$ electron from Kr^{2+} is closed (see Table 1, lines 13–17). Therefore, the two-photon resonance ionization might occur in the latter case. Nevertheless, we neglect this process, because it can proceed for Kr^{2+} at photon energies around 50 eV only via high Rydberg states with small excitation and ionization probability. For the photon energies higher than $\sim$58 eV all the $4s$ ionization channels for Kr^{2+} open and the two photon resonance ionization channels disappear.

We assume a temporal Gaussian distribution of the incident photon flux density (number of photons per surface per time):

$$j(t) = j_0 \, \exp(-t^2/t_p^2) \,, \tag{4}$$

where t_p is related to the full width at half maximum (FWHM) of the pulse, FWHM $= 2\sqrt{\ln 2} \, t_p$. The photon flux is related to the fluence F, i.e., to the integral number of photons per 1 Å^2 in the entire pulse, as

$$j_0 = \frac{2\sqrt{\ln 2} \, F}{\sqrt{\pi} \, \text{FWHM}} = 0.0063634 \, \frac{F \, [\text{ph}/\text{Å}^2]}{\text{FWHM} \, [\text{fs}]} \,. \tag{5}$$

Equation (5) is obtained by considering the integral of (4) over time and transforming from atomic units.

For a fixed fluence, Equations (3) are invariant under changes of the time scale, $t \to at$, where a is a constant. This scaling feature breaks down when additional terms not proportional to $j(t)$, such as fluorescence and Auger decays, are added to the right side of (3). Thus, the calculations for a fixed fluence can be performed for a generic pulse duration and then scaled. Our case differs in this respect substantially from previous calculations, where the competing Auger decay had to be included and each pulse duration had to be calculated individually. In this paper we fix the pulse duration to $t_p = 18$ fs (FWHM = 30 fs), which is comparable to the typical pulse duration obtained at the seeded FEL FERMI [33,34].

In order to predict the electron spectrum generated by the pulse, we calculate the probability $P_{ij}(F)$ (which depends on the fluence F) that an ion (atom) in a state i is ionized into the ion in a state j over the entire pulse and build up the function,

$$f_F(\varepsilon) = \sum_{ij} P_{ij}(F) \exp[-(\varepsilon + I_{ij} - \omega)^2/\Gamma^2] \,, \tag{6}$$

where ε is the kinetic energy of the photoelectron at the photon energy ω, I_{ij} is the threshold of ionization of the state i to the state j (binding energy) and Γ represents the resolution of the electron detector. We assumed $\Gamma = 0.42$ eV (corresponding to the resolution FWHM = 0.7 eV), in order to leave the fine structure of levels unresolved, as explained above.

3. Results and Discussion

Our main results are presented in Figures 2 and 3 for the population of the different ionic states and Figure 4 for the photoelectron spectra.
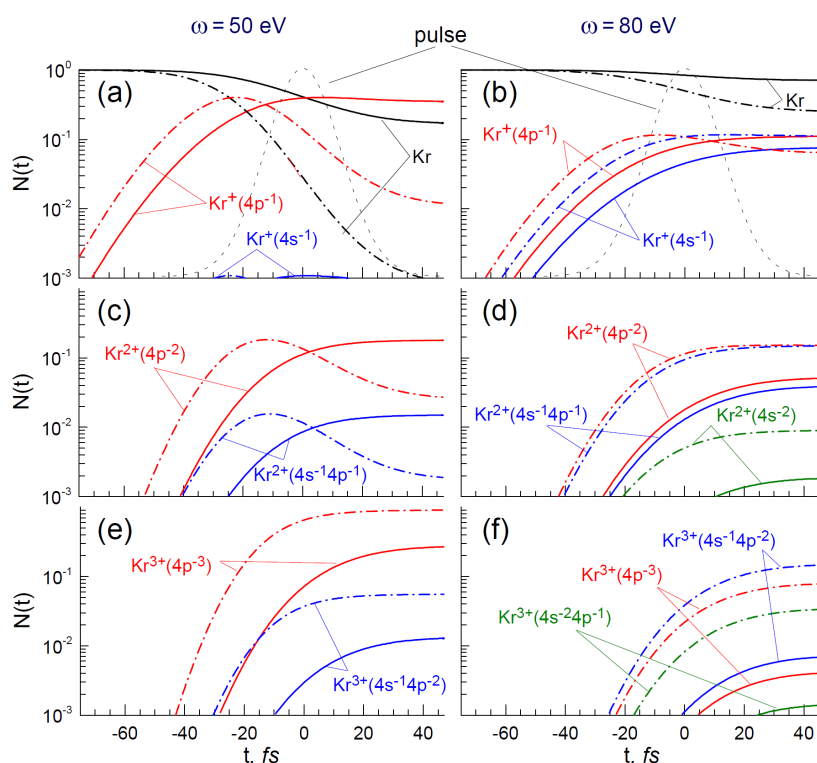
Figure 2. Population of different ion charge states and configurations for two fluences: $F = 100$ ph/Å^2 (solid lines) and $F = 400$ ph/Å^2 (dash-dotted line) for the photon energies 50 eV (**a,c,e**) and 80 eV (**b,d,f**). Black lines—ionization of neutral Kr; red lines—ionization to $4s^24p^{-n}$ configuration, where n is the ion charge; blue lines—ionization to $4s^{-1}4p^{-n+1}$, green lines—ionization to $4s^{-2}4p^{-n+2}$. The pulse envelope (grey dashed line) is indicated in the upper panels.
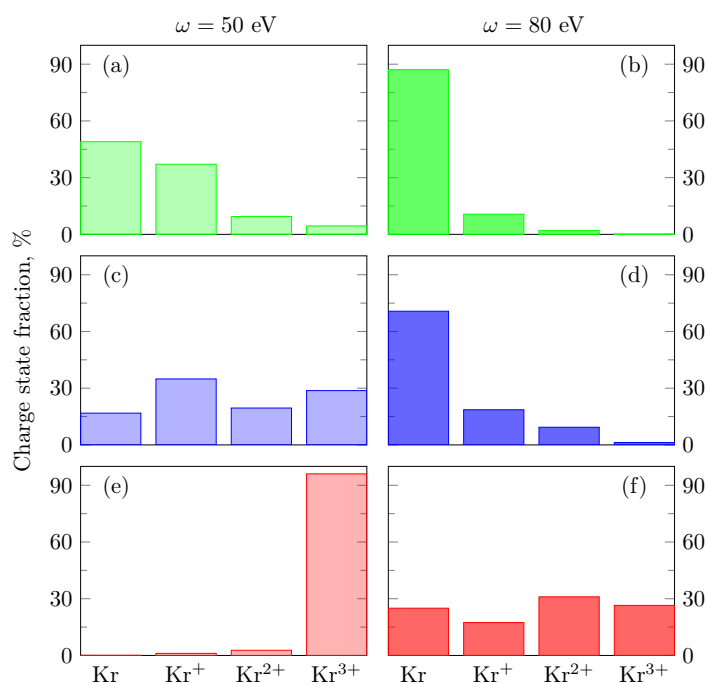
Figure 3. Charge-state yields for three fluences: $F = 40$ ph/Å^2 (**a,b**), $F = 100$ ph/Å^2 (**c,d**), and $F = 400$ ph/Å^2 (**e,f**) for the photon energies 50 eV (**a,c,e**) and 80 eV (**b,d,f**).
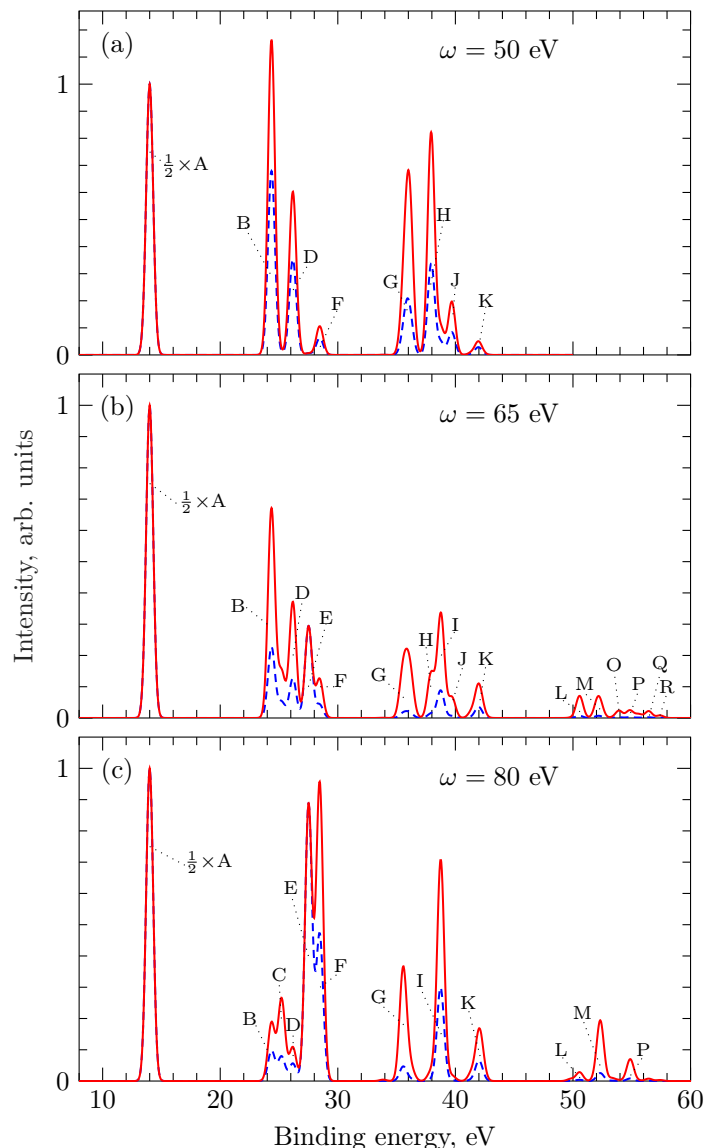
Figure 4. Photoelectron spectrum for different photon energy: $\omega = 50$ eV (**a**), $\omega = 65$ eV (**b**), and $\omega = 80$ eV (**c**). Solid lines: $F = 400$ ph/Å^2; dashed lines: $F = 100$ ph/Å^2. The spectra are normalized in such a way that $1/2$ of the main line A equals unity. The spectral features are indicated by capital letters in accordance with Table 1.

3.1. Time Evolution of Population

In Figure 2, we present results obtained with 50 eV (left column) and 80 eV (right column) photon energies and fluences $F = 100$ ph/Å^2 (solid lines) and $F = 400$ ph/Å^2 (dash-dotted lines). We summed up over the populations of different terms within one configuration.

The population of the ionic states Kr$^+$, Kr^{2+} and Kr^{3+} is presented as a function of time in the first, second and third rows, respectively. Different colors correspond to the configurations without $4s$-hole (red), with one $4s$-hole (blue) and double $4s$-hole (green). With the value of $t_p = 18$ fs the above fluences correspond to intensities between 10^{15} and 10^{16} W/cm^2. As explained above, the curves in Figure 2 remain the same for fixed values of F, after appropriate scaling of the pulse duration and of the timescale. In particular, the final populations of the levels at the end of the pulses are invariant for changes of the pulse duration (for a fixed fluence).

For the photon energy of 50 eV, ionization of the valence $4p$ shell dominates; the configurations Kr^{n+} $4s^2 4p^{-n}$ (red curves in Figure 2a,c,e) are quickly populated, reaching maximum of the population

at slightly different times, depending on the ionic charge and the fluence. As expected, the population maxima are reached at later instants for increasing ionic charge states and decreasing pulse fluences. At the end of the pulse, the populations become constants, because the Auger decay of the holes is energetically forbidden and the fluorescence occur on much longer time scale. The sum of all values presented in Figure 2a,c,e, as well as in Figure 2b,d,f corresponding to the same conditions (time, fluence, photon energy) equals unity.

For the fluence of $F = 400$ ph/Å^2, the majority of the krypton atoms, $\sim$90.5%, are found after the pulse in the triply charged ionic state in its ground configuration Kr^{3+} $4s^2 4p^3$ (Figure 2e). Configurations of ions with one 4s-hole are populated on the level of $\sim$5.5%, while the amount of ions Kr^{2+} and Kr^{3+} with double 4s-holes is negligible. This result is explained by the very small 4s ionization cross section in the region of the Cooper minimum around 45 eV (see Section 4). The concentration of neutral atoms at the end of the pulse is also negligible (Figure 2a). The number of singly and doubly charged ions first increases with time, but then it drops down (Figure 2a,c), because the fluence is high enough to further ionize them to Kr^{3+} within the pulse.

For the smaller fluence of $F = 100$ ph/Å^2, already 17% of atoms are left as neutrals (Figure 2a) and the ions are distributed between singly, doubly and triply charged ions with the corresponding concentrations of 35%, 20%, and 29% (Figure 2a,c,e), dominated by ions without 4s-holes. At this lower fluence the population of states increases smoothly with time, without showing pronounced maxima.

For the photon energy of 80 eV, the final concentration of the neutral atoms is much higher (compare Figure 2a,b) than for the photon energy of 50 eV, because the 4p ionization cross section rapidly decreases with the photon energy in interval from 50 eV to 80 eV. At the same time, the production of ions with the 4s-vacancy is much more efficient, because the 4s ionization cross section increases in this energy interval, which is just above the corresponding Cooper minimum. At $F = 400$ ph/Å^2 the number of the Kr ions after the pulse in each charge state with a 4s-hole exceeds the number of the ions with only 4p ionized electrons. Furthermore, the number of Kr ions with the double 4s-hole reaches 4.5% of all the target atoms.

Finally, in Figure 3 we present the overall ionic yields at fluences $F = 40$ ph/Å^2, $F = 100$ ph/Å^2 and $F = 400$ ph/Å^2 and photon energies $\omega = 50$ eV and $\omega = 80$ eV. The population of the different ionic states strongly depends on the photon energy and fluence. Figure 3a,b,d show a typical situation for multiple ionization in a regime far from saturation, when the ions with higher charge have smaller yields. Although ionization of Kr^{3+} is energetically possible for 80 eV photons, Figure 3b,d show that at the fluences of $F = 40$ ph/Å^2 and $F = 100$ ph/Å^2 the contribution of higher charge states is negligible. The opposite behavior is shown in Figure 3e, in which nearly all ions are in highest allowed charged state, because a further ionization step is energetically forbidden for the photon energy of 50 eV. In this case the intensity of the radiation and the cross section of the 4p-ionization are high enough to promote three 4p electrons into the continuum during the pulse. More uniform distribution in Figure 3c,f show an intermediate regime, caused by an interplay between energy dependence of the ionization cross sections and fluence. Note that the last column in Figure 3f actually presents the sum yield ($\sim$25%) of ions with charges three and higher. Although we cut the treatment at Kr^{3+}, the photoelectron spectra presented below, are not influenced by this fact in the considered interval of the electron energies.

3.2. Photoelectron Spectra

The photoelectron spectrum contains much more information on the pathways of the sequential ionization than the ion yield, because it gives information on the relative population of the intermediate states of the process (see Figure 1 and Table 1). This information becomes more detailed by improving the energy resolution of the electron detector and decreasing the pulse spectral bandwidth.

The generated photoelectron spectra for three photon energies, 50 eV, 65 eV, and 80 eV are displayed in Figure 4a–c, respectively.

We considered the modifications of the spectra in a broad range of photon fluences. Figure 4a–c show, as examples, spectra for the two fluences, $F = 100$ ph/Å^2 and $F = 400$ ph/Å^2. As follows from Table 1, lines A and E originate from single ionization of Kr and are produced by absorption of one photon. Lines B, C, D, and F are due to one-photon ionization of Kr$^+$ and, therefore, in the sequential two-photon double ionization of Kr. Lines G, H, J, L–R are produced in the sequential three-photon triple ionization of Kr. Lines I and K represent an overlap between a few lines from the sequential two- and three-photon ionization. In Figure 4a–c the lines are concentrated in certain groups: three groups for the photon energy of 50 eV and four groups for the photon energies 65 eV and 80 eV. The three groups at $\omega = 50$ eV (Figure 4a) correspond to the line from the 4p-shell ionization of neutral Kr (electron energy 36 eV), lines from ionization of mostly Kr$^+$ 4$s^2$4p^5 (electron energies 21–26 eV) and from ionization of mostly Kr^{2+} 4$s^2$4p^4 (electron energies 8–14 eV). The fourth group of lines appears at the photon energies 65 eV and 80 eV (Figure 4b,c), when ionization of the 4s-electron from Kr^{2+} 4$s^2$4p^4 and Kr^{2+} 4$s^1$4p^5 is opened. Note that some of the lines in different panels of Figure 4 are not indicated because of negligible contributions to the spectra.

Comparison of Figure 4a,b shows that the intensity of the photoelectron lines drops down for increasing ionic charges at the photon energy of 65 eV faster than at 50 eV, for a fixed fluence. This is caused by the decrease of the 4p-subshell ionization cross-section with increasing photon energy in this range (see Section 4). For higher photon energies the role of the multiple ionization increases (Figure 4c), due to the increase of the ionization cross-section of the 4s-subshell after the corresponding Cooper minimum (see Section 4, Figure 5b). The change of the relative contribution of 4s- and 4p-ionization channels leads to substantial modifications of the photoelectron spectrum. For example, lines E and I with large contribution from the 4s-ionization, are not observed at $\omega = 50$ eV, but dominate in their group at $\omega = 80$ eV. This is opposite to neon, where ionization from the subvalence 2s shell modifies noticeably the photoelectron spectrum at all photon energies within the (ii) regime [10,15]. We expect that the interference Cooper minimum in the 3s-ionization of Ar around $\omega = 40$ eV [35,36], leads to modifications of the spectra as function of the photon energy similar to the present Kr case.

Figure 6 shows the fluence dependence of the intensities of some selected spectral lines. The curves clearly indicate the one-, two- and three-photon origin of the spectral features A and EF, I and BCD, and G, respectively. The saturation starts to show up at fluences above 100 ph/Å^2, progressing from the first (one-photon) to the third (three-photon) steps of the sequential ionization process.
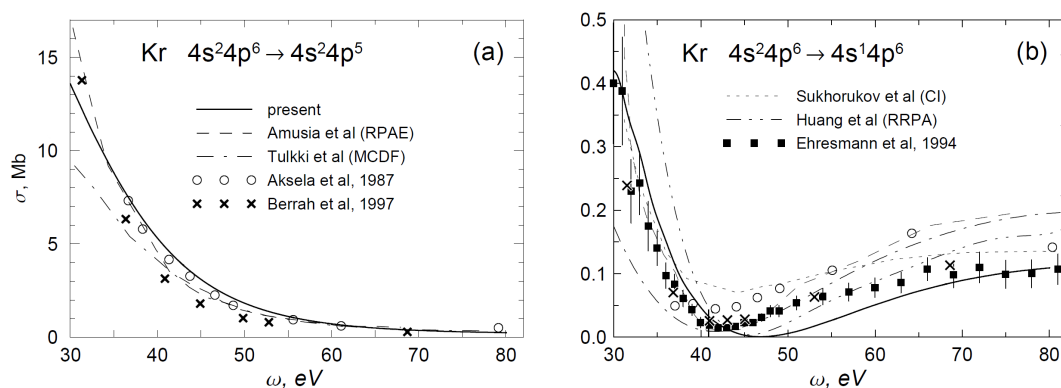

Figure 5. Photoionization cross-sections for the 4p (**a**) and 4s (**b**) level of Kr. Solid curves — present calculations. Other curves: random phase approximation with exchange (RPAE) from [37] (dashed curve), multichannel Dirac-Fock (MCDF) approximation from [38] (dash-dotted curve), configuration interaction (CI) approximation from [39] (short-dashed curve), relativistic random phase approximation (RRPA) from [40] (dash-dot-dot curve). Experimental data from [41] (squares), [42] (crosses), and [43] (open circles).
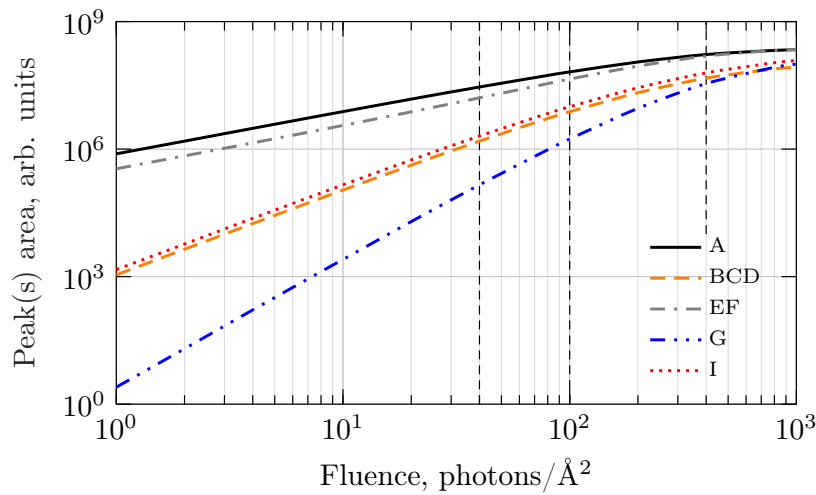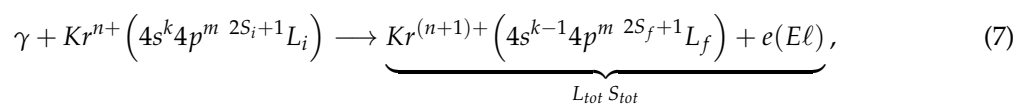
Figure 6. Intensity dependence of different photoelectron lines on the fluence F for the photon energy $\omega = 80$ eV. Vertical dashed lines indicate fluences related to Figures 2–4: 40 ph/Å^2, 100 ph/Å^2, and 400 ph/Å^2.

4. Method of the Cross Section Calculations

Photoionization cross sections of multiplet states $4s^k 4p^{m\ 2S+1}L$ for variously charged Kr ions were calculated by the B-spline R-matrix approach [44], which fully takes into account non-orthogonality of the electron functions before and after the ionization. For all the three steps, the basis wave functions of each of the initial nine states listed in Table 1 were obtained in independent Hartee-Fock calculations in the LS-coupling approximation with variation of $4s$ and $4p$ orbitals and the $1s^2 2s^2 2p^6 3s^2 3p^6 3d^{10}$ Ar-like core frozen from the self-consistent calculations for the ground state of Kr. The final ionic states (numbers 2–17 in Table 1) were similarly calculated in independent Hartree-Fock calculations with variable $4s$ and $4p$ electron orbitals. For each step, the corresponding set of final ionic states were included in the R-matrix expansion, giving the total angular momentum L_{tot} and spin S_{tot} of the system (final ion + electron) satisfying the dipole selection rules. Overall 19 R-matrix runs were needed for the reactions of the type

$$\gamma + Kr^{n+}\left(4s^k 4p^{m\ 2S_i+1}L_i\right) \longrightarrow \underbrace{Kr^{(n+1)+}\left(4s^{k-1}4p^{m\ 2S_f+1}L_f\right) + e(E\ell)}_{L_{tot}\,S_{tot}}, \tag{7}$$

where n = 0, 1, 2 and ℓ are the orbital angular momentum of the photoelectron. Each of the reactions (7) describes a few ionization channels with one of the fixed nine initial states from Table 1 and fixed values of $L_{tot}S_{tot}$, but all possible from 17 final $Kr^{(n+1)+}$ states and ℓ. The ionization cross section to a particular final ionic state is obtained by summation over all corresponding channels with different sets of ℓ, L_{tot}, S_{tot}.

Figure 5 presents photoionization cross sections of the $4p$ (Figure 5a) and $4s$ (Figure 5b) electrons from Kr $4s^2 4p^{6\ 1}S$, respectively, i.e., for the first step of the sequential ionization. These cross sections can be compared with experiment and other calculations [35,37–43,45,46]. Here and below we use results in the velocity gauge which better agrees with experiment for neutral Kr.

Ionization cross sections for the second step into different multiplet states of the doubly charged ion are shown in Figure 7: ionization from Kr$^+$ $4s^2 4p^{5\ 2}P^o$ and from Kr$^+$ $4s 4p^{6\ 2}S$ are displayed in Figure 7a,b, respectively. Figure 8 is related to the third step and shows ionization cross sections from six multiplet states of Kr^{2+} to different multiplet states of Kr^{3+}. The transitions correspond to those indicated in Table 1.
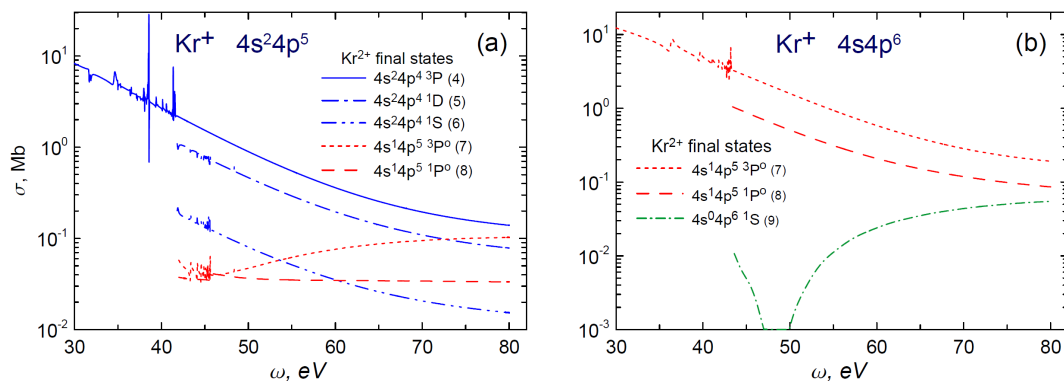
Figure 7. Photoionization cross-sections from the $4s^24p^5\,^2P^o$ (**a**) and $4s^14p^6\,^2S$ state (**b**) of Kr$^+$. Legends for the curves with the corresponding final Kr^{2+} multiplet states and their numbers (in parenthesis) according to Table 1 are presented. The blue lines in (**a**) correspond to ionization of the $4p$ electron into different terms of the Kr^{2+} $4s^24p^4$ configuration. The green dash-dotted line in (**b**) corresponds to producing of the double-hole state Kr^{2+} $4s^04p^6$. Identical red lines in the both panels show transitions to the same final states from Kr$^+$ $4s^24p^5$ (panel (**a**)) and Kr$^+$ $4s4p^6$ (panel (**b**)), respectively.
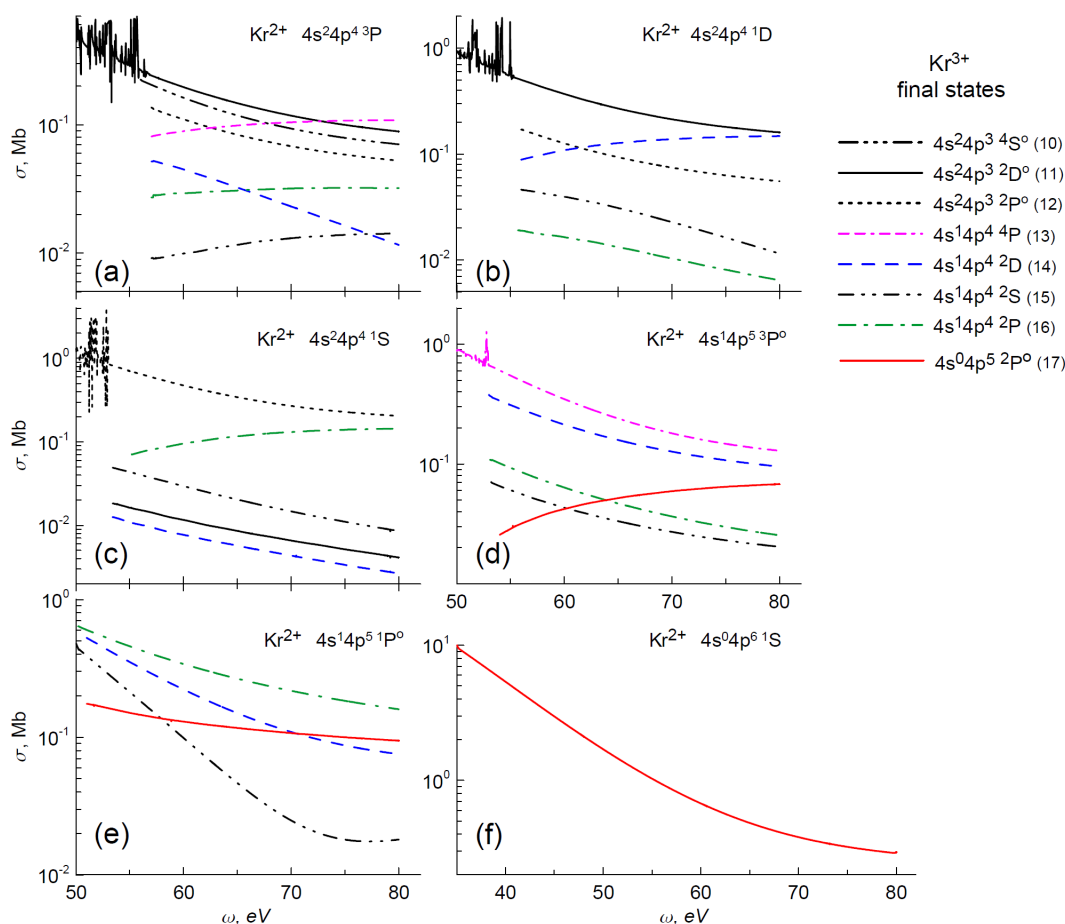

Figure 8. Photoionization cross-sections from different multiplet states of Kr^{2+}. indicated in the panels. Legends for the curves with the corresponding final Kr^{3+} states and their numbers (in parenthesis) according to Table 1 are presented at the right. (See text).

Ionization cross section of a subvalence $4s$ shell in Kr shows a deep interference Cooper minimum around the photon energy of 45 eV [35] (Figure 5b). The position and the depth of the minimum is

very sensitive to the model. In our study the particular value of the $4s$ ionization cross section in the minimum is not so important except the fact that it is at least two orders of magnitude less than the $4p$ ionization cross section. The Cooper minimum occurs in the $4s$ ionization from the Kr^+ $4s^1 4p^6$ state (Figure 7b, green line), but looks moving under the threshold in ionization from the Kr^+ $4s^2 4p^5$ state (Figure 7a, red lines). In the ionization of the doubly charged ion, the appearance of the Cooper minimum strongly depends on the initial and final ion configurations (Figure 8).

There are series of Rydberg autoionizing states with configurations $4s^n 4p^m (^{2S_f+1}L_f) np$ in the energy region under consideration. The series appear in the ionization of $4p$ shell at photon energy below the $4s$ ionization threshold for all terms and configurations with only one exception, $4s^0 4p^m$. Besides, the Rydberg series appear in the ionization of $4s$ shell between the split multiplet thresholds, for example between $4s4p^5$ $^3P^o$ and $4s4p^5$ $^1P^o$. For the sake of clarity, in Figures 7 and 8, we show only sample resonance structures on the upper curves, obtained in our R-matrix calculations, cutting other curves in the near-threshold region in other cases. Although our calculations automatically accounts for the autoionizing resonances, a careful analysis showed that with the currently available spectral width of intense XUV pulses and the electron detector resolution, it is hardly possible to observe resonance effects in integrated observables such as ionic or electron yields. In order to reveal these resonances, more detailed measurements like photoelectron angular distribution [10,47] or angular correlation functions [18] are needed.

5. Conclusions

Time eVolution and photoelectron spectra in sequential photoionization of atomic krypton by intense femtosecond XUV pulses at the photon energies from 50 eV to 80 eV are studied theoretically. In this regime the Auger decay channel is closed and the ionization proceeds through photoemission of $4s$ and $4p$ electrons. Within our model, the results are applicable to pulses with arbitrary duration within the femtosecond domain, due to the time scaling of the rate equations. Lines from single, double and triple ionization processes are predicted in the photoelectron spectra. The intensity of the lines is proportional to the corresponding power of the fluence up to the saturation fluence of about 10^2 ph/$Å^2$. The Cooper minimum in the $4s$ ionization cross section influences the time eVolution of the target and eVolution of the photoelectron spectrum with the photon energy. Nevertheless, the population of states with the $4s$-hole after the pulse can reach tens percents. The present study is a natural step before turning to higher photon energies, when the $3d$ excitation threshold is opened and the Auger decay makes the dynamics more complex.

References

1. Sorokin, A.A.; Bobashev, S.V.; Feigl, T.; Tiedtke, K.; Wabnitz, H.; Richter, M. Photoelectric Effect at Ultrahigh Intensities. *Phys. Rev. Lett.* **2007**, *99*, 213002. [CrossRef]
2. Young, L.; Kanter, E.P.; Krässig, B.; Li, Y.; March, A.M.; Pratt, S.T.; Santra, R.; Southworth, S.H.; Rohringer, N.; DiMauro, L.F.; et al. Femtosecond electronic response of atoms to ultra-intense X-rays. *Nature* **2010**, *466*, 56–61. [CrossRef]

3. Southworth, S.H.; Dunford, R.W.; Ray, D.; Kanter, E.P.; Doumy, G.; March, A.M.; Ho, P.J.; Krässig, B.; Gao, Y.; Lehmann, C.S.; et al. Observing pre-edge K-shell resonances in Kr, Xe, and XeF$_2$. *Phys. Rev. A* **2019**, *100*, 022507. [CrossRef]

4. Berrah, N.; Fang, L.; Osipov, T.; Murphy, B.; Bostedtc, C.; Bozek, J. Multiphoton ionization and fragmentation of molecules with the LCLSX-ray FEL. *J. Electron Spectrosc. Relat. Phenom.* **2014**, *196*, 34–37. [CrossRef]

5. Fushitani, M.; Sasaki, Y.; Matsuda, A.; Fujise, H.; Kawabe, Y.; Hashigaya, K.; Owada, S.; Togashi, T.; Nakajima, K.; Yabashi, M.; et al. Multielectron-Ion Coincidence Spectroscopy of Xe in Extreme Ultraviolet Laser Fields: Nonlinear Multiple Ionization via Double Core-Hole States. *Phys. Rev. Lett.* **2020**, *124*, 193201. [CrossRef]

6. Kurka, M.; Rudenko, A.; Foucar, L.; Kühnel, K.U.; Jiang, Y.H.; Ergler, T.; Havermeier, T.; Smolarski, M.; Schössler, S.; Cole, K.; et al. Two-photon double ionization of Ne by free-electron laser radiation: A kinematically complete experiment. *J. Phys. B At. Mol. Opt. Phys.* **2009**, *42*, 141002. [CrossRef]

7. Mondal, S.; Ma, R.; Motomura, K.; Fukuzawa, H.; Yamada, A.; Nagaya, K.; Yase, S.; Mizoguchi, Y.; Yao, M.; Rouzée, A.; et al. Photoelectron angular distributions for the two-photon sequential double ionization of xenon by ultrashort extreme ultraviolet free electron laser pulses. *J. Phys. B At. Mol. Opt. Phys.* **2013**, *46*, 164022. [CrossRef]

8. Braune, M.; Hartmann, G.; Ilchen, M.; Knie, A.; Lischke, T.; Reinköster, A.; Meissner, A.; Deinert, S.; Glaser, L.; Al-Dossary, O.; et al. Electron angular distributions of noble gases in sequential two-photon double ionization. *J. Mod. Opt.* **2016**, *63*, 324. [CrossRef]

9. Ilchen, M.; Hartmann, G.; Gryzlova, E.V.; Achner, A.; Allaria, E.; Beckmann, A.; Braune, M.; Buck, J.; Callegari, C.; Coffee, R.N.; et al. Symmetry breakdown of electron emission in extreme ultraviolet photoionization of argon. *Nat. Commun.* **2018**, *8*, 4659. [CrossRef]

10. Carpeggiani, P.A.; Gryzlova, E.V.; Reduzzi, M.; Dubrouil, A.; Facialá, D.; Negro, M.; Ueda, K.; Burkov, S.M.; Frassetto, F.; Stienkemeier, F.; et al. Complete reconstruction of bound and unbound electronic wavefunctions in two-photon double ionization. *Nat. Phys.* **2019**, *15*, 170–177. [CrossRef]

11. Kheifets, A.S. Sequential two-photon double ionization of noble gas atoms. *J. Phys. B At. Mol. Opt.* **2007**, *40*, F313–F318. [CrossRef]

12. Fritzsche, S.; Grum-Grzhimailo, A.N.; Gryzlova, E.V.; Kabachnik, N.M. Angular distributions and angular correlations in sequential two-photon double ionization of atoms. *J. Phys. B At. Mol. Opt. Phys.* **2008**, *41*, 165601. [CrossRef]

13. Fritzsche, S.; Grum-Grzhimailo, A.N.; Gryzlova, E.V.; Kabachnik, N.M. Sequential two-photon double ionization of Kr atoms. *J. Phys. B At. Mol. Opt. Phys.* **2009**, *42*, 145602. [CrossRef]

14. Grum-Grzhimailo, A.N.; Gryzlova, E.V.; Meyer, M. Non-dipole effects in the angular distribution of photoelectrons in sequential two-photon atomic double ionization. *J. Phys. B At. Mol. Opt. Phys.* **2012**, *45*, 215602. [CrossRef]

15. Rouzee, A.; Johnsson, P.; Gryzlova, E.; Fukuzawa, H.; Yamada, A.; Siu, W.; Huismans, Y.; Louis, E.; Bijkerk, F.; Holland, D.; et al. Angle-resolved photoelectron spectroscopy of sequential three-photon triple ionization of neon at 90.5 eV photon energy. *Phys. Rev. A* **2011**, *83*, 031401(R). [CrossRef]

16. Gryzlova, E.V.; Grum-Grzhimailo, A.N.; Fritzsche, S.; Kabachnik, N.M. Angular correlations between two electrons emitted in the sequential two-photon double ionization of atoms. *J. Phys. B At. Mol. Opt. Phys.* **2010**, *43*, 225602. [CrossRef]

17. Gryzlova, E.V.; Ma, R.; Fukuzawa, H.; Motomura, K.; Yamada, A.; Ueda, K.; Grum-Grzhimailo, A.N.; Kabachnik, N.M.; Strakhova, S.I.; Rouzée, A.; et al. Doubly resonant three-photon double ionization of Ar atoms induced by an EUV free-electron laser. *Phys. Rev. A* **2011**, *84*, 063405. [CrossRef]

18. Augustin, S.; Schulz, M.; Schmid, G.; Schnorr, K.; Gryzlova, E.V.; Lindenblatt, H.; Meister, S.; Liu, Y.F.; Trost, F.; Fechner, L.; et al. Signatures of autoionization in the angular electron distribution in two-photon double ionization of Ar. *Phys. Rev. A* **2018**, *98*, 033408. [CrossRef]

19. Grum-Grzhimailo, A.N.; Gryzlova, E.V.; Fritzsche, S.; Kabachnik, N.M. Photoelectron angular distributions and correlations in sequential double and triple atomic ionization by free electron lasers. *J. Mod. Opt.* **2016**, *60*, 334–357. [CrossRef]

20. King, G.C.; Tronc, M.; Read, F.H.; Bradford, R.C. An investigation of the structure near the L$_{2,3}$ edges of argon, the M$_{4,5}$ edges of krypton and the N$_{4,5}$ edges of xenon, using electron impact with high resolution. *J. Phys. B At. Mol. Phys.* **1977**, *10*, 2479–2495. [CrossRef]

21. *NIST Atomic Spectra Database (Version 5.7.1)*; National Institute of Standards and Technology: Gaithersburg, MD, USA, 2019. Available online: https://physics.nist.gov/asd (accessed on 9 November 2020).
22. Nakajima, T.; Nikolopoulos, L.A.A. Use of helium double ionization for autocorrelation of an xuv pulse. *Phys. Rev. A* **2002**, *66*, 041402R. [CrossRef]
23. Makris, M.G.; Lambropoulos, P.; Mihelič, A. Theory of Multiphoton Multielectron Ionization of Xenon under Strong 93-eV Radiation. *Phys. Rev. Lett.* **2009**, *102*, 033002. [CrossRef] [PubMed]
24. Son, S.K.; Santra, R. Impact of hollow-atom formation on coherent x-ray scattering at high intensity. *Phys. Rev. A* **2011**, *83*, 033402. [CrossRef]
25. Son, S.K.; Santra, R. Monte Carlo calculation of ion, electron, and photon spectra of xenon atoms in X-ray free-electron laser pulses. *Phys. Rev. A* **2012**, *85*, 063415. [CrossRef]
26. Lorenz, U.; Kabachnik, N.M.; Weckert, E.; Vartanyants, I.A. Impact of ultrafast electronic damage in single-particle x-ray imaging experiments. *Phys. Rev. E* **2012**, *86*, 051911. [CrossRef] [PubMed]
27. Lunin, V.Y.; Grum-Grzhimailo, A.N.; Gryzlova, E.V.; Sinitsyn, D.O.; Petrova, T.E.; Lunina, N.L.; Balabaev, N.K.; Tereshkina, K.B.; Stepanov, A.S.; Krupyanskii, Y.F. Efficient calculation of diffracted intensities in the case of nonstationary scattering by biological macromolecules under XFEL pulses. *Acta Cryst. D* **2015**, *71*, 293–303. [CrossRef]
28. Serkez, S.; Geloni, G.; Tomin, S.; Feng, G.; Gryzlova, E.V.; Grum-Grzhimailo, A.N.; Meyer, M. Overview of options for generating high-brightness attosecond x-ray pulses at free-electron lasers and applications at the European XFEL. *J. Opt.* **2018**, *20*, 024005. [CrossRef]
29. Buth, C.; Beerwerth, R.; Obaid, R.; Berrah, N.; Cederbaum, L.S.; Fritzsche, S. Neon in ultrashort and intense x-rays from free electron lasers. *J. Phys. B At. Mol. Opt. Phys.* **2018**, *51*, 055602. [CrossRef]
30. Ilchen, M.; Mazza, T.; Karamatskos, E.T.; Markellos, D.; Bakhtiarzadeh, S.; Rafipoor, A.J.; Kelly, T.J.; Walsh, N.; Costello, J.T.; O'Keeffe, P.; et al. Two-electron processes in multiple ionization under strong soft-X-ray radiation. *Phys. Rev. A* **2016**, *94*, 013413. [CrossRef]
31. Rudek, B.; Son, S.K.; Foucar, L.; Epp, S.W.; Erk, B.; Hartmann, R.; Adolph, M.; Andritschke, R.; Aquila, A.; Berrah, N.; et al. Ultra-efficient ionization of heavy atoms by intense X-ray free-electron laser pulses. *Nat. Photonics* **2012**, *6*, 858–865. [CrossRef]
32. Rudek, B.; Rolles, D.; Son, S.K.; Foucar, L.; Erk, B.; Epp, S.; Boll, R.; Anielski, D.; Bostedt, C.; Schorb, S.; et al. Resonance-enhanced multiple ionization of krypton at an x-ray free-electron laser. *Phys. Rev. A* **2013**, *87*, 023413. [CrossRef]
33. Allaria, E.; Appio, R.; Badano, L.; Barletta, W.A.; Bassanese, S.; Biedron, S.G.; Borga, A.; Busetto, E.; Castronovo, D.; Cinquegrana, P.; et al. Highly coherent and stable pulses from the FERMI seeded free-electron laser in the extreme ultraviolet. *Nat. Photonics* **2012**, *6*, 699–704. [CrossRef]
34. Finetti, P.; Höppner, H.; Allaria, E.; Callegari, C.; Capotondi, F.; Cinquegrana, P.; Coreno, M.; Cucini, R.; Danailov, M.B.; Demidovich, A.; et al. Pulse Duration of Seeded Free-Electron Lasers. *Phys. Rev. X* **2017**, *7*, 021043. [CrossRef]
35. Amusia, M.Y.; Ivanov, V.K.; Cherepkov, N.A.; Chernysheva, L.V. Interference effects in photoionization of noble gas atoms outer s-shells. *Phys. Lett.* **1972**, *40A*, 361–362. [CrossRef]
36. Lynch, M.J.; Gardner, A.B.; Codling, K.; Marr, G.V. The photoionization of the 3s subshell of argon in the threshold region by photoelectron spectroscopy. *Phys. Lett.* **1973**, *43A*, 237–238. [CrossRef]
37. Amusia, M.; Chernysheva, L.; Yarzhemsky, V. *Handbook of Theoretical Atomic Physics: Data for Photon Absorption, Electron Scattering, and Vacancies Decay*; Springer Science & Business Media: Berlin, Germany, 2012.
38. Tulkki, J.; Aksela, S.; Aksela, H.; Shigemasa, E.; Yagishita, A.; Furusawa, Y. Krypton 4p, 4s, and 3d partial photoionization cross sections below a photon energy of 260 eV. *Phys. Rev. A* **1992**, *45*, 4640–4645. [CrossRef]
39. Sukhorukov, V.L.; Lagutin, B.M.; Petrov, I.D.; Schmoranzer, H.; Ehresmann, A.; Schartner, K.H. Photoionization of Kr near 4s threshold. II. Intermediate-coupling theory. *J. Phys. B At. Mol. Opt. Phys.* **1994**, *27*, 241–256. [CrossRef]
40. Huang, K.N.; Johnson, W.; Cheng, K. Theoretical photoionization parameters for the noble gases argon, krypton, and xenon. *At. Data Nucl. Data Tables* **1981**, *26*, 33–45. doi:10.1016/0092-640X(81)90010-3. [CrossRef]
41. Ehresmann, A.; Vollweiler, F.; Schmoranzer, H.; Sukhorukov, V.L.; Lagutin, B.M.; Petrov, I.D.; Mentzel, G.; Schartner, K.H. Photoionization of Kr 4s: III. Detailed and extended measurements of the Kr 4s-electron ionization cross section. *J. Phys. B At. Mol. Opt. Phys.* **1994**, *27*, 1489–1496. [CrossRef]

42.   Berrah, N.; Farhat, A.; Langer, B.; Lagutin, B.M.; Demekhin, P.V.; Petrov, I.D.; Sukhorukov, V.L.; Wehlitz, R.; Whitfield, S.B.; Viefhaus, J.; et al. Angle-resolved energy dependence of the $4p^4nd(^2S_{1/2})$ ($n = 4$–7) correlation satellites in Kr from 38.5 to 250 eV: Experiment and theory. *Phys. Rev. A* **1997**, *56*, 4545–4553. [CrossRef]

43.   Aksela, S.; Aksela, H.; Levasalmi, M.; Tan, K.H.; Bancroft, G.M. Partial photoionization cross sections of Kr 3d, 4s, and 4p levels in the photon energy range 37–160 eV. *Phys. Rev. A* **1987**, *36*, 3449–3450. [CrossRef] [PubMed]

44.   Zatsarinny, O. BSR: B-spline atomic R-matrix codes. *Comput. Phys. Commun.* **2006**, *174*, 273–356. [CrossRef]

45.   Samson, J.A.R.; Gardner, J.L. Photoionization Cross Sections of the Outer *s*-Subshell Electrons in the Rare Gases. *Phys. Rev. Lett.* **1974**, *33*, 671–673. [CrossRef]

46.   Johnson, W.R.; Cheng, K.T. Photoionization of the outer shells of neon, argon, krypton, and xenon using the relativistic random-phase approximation. *Phys. Rev. A* **1979**, *20*, 978–988. [CrossRef]

47.   Kiselev, M.D.; Carpeggiani, P.A.; Gryzlova, E.V.; Burkov, S.M.; Reduzzi, M.; Dubrouil, A.; Facciala, D.; Negro, M.; Ueda, K.; Frassetto, F.; et al. Photoelectron spectra and angular distribution in sequential two-photon double ionization in the region of autoionizing resonances of ArII and KrII. *J. Phys. B At. Mol. Phys.* **2020**, accepted. [CrossRef]